



# Geothermal heat flux distribution for the Greenland ice sheet, derived by combining a global representation and information from deep ice cores

Ralf GREVE<sup>1\*</sup>

<sup>1</sup>Institute of Low Temperature Science, Hokkaido University, Kita-19, Nishi-8, Kita-ku, Sapporo 060-0819, Japan.

\*Corresponding author (greve@lowtem.hokudai.ac.jp)  
(Received July 20, 2018; Accepted January 30, 2019)

**Abstract:** We present a distribution of the geothermal heat flux (GHF) for Greenland, which is an update of two earlier versions by Greve (2005, *Ann. Glaciol.* 42) and Greve and Herzfeld (2013, *Ann. Glaciol.* 54). The GHF distribution is constructed in two steps. First, the global representation by Pollack *et al.* (1993, *Rev. Geophys.* 31) is scaled for the area of Greenland. Second, by means of a paleoclimatic simulation carried out with the ice sheet model SICOPOLIS, the GHF values for five deep ice core locations are modified such that observed and simulated basal temperatures match closely. The resulting GHF distribution generally features low values in the south and the north-west, whereas elevated values prevail in central North Greenland and towards the north-east. The data are provided as NetCDF files on two different grids (EPSG:3413 grid, Bamber grid) that have frequently been used in modelling studies of the Greenland ice sheet, and for the three different resolutions of 5 km, 10 km and 20 km.

## 1. Background & Summary

The geothermal heat flux (GHF) under the Greenland ice sheet is an important parameter that controls the ice flow via the thermal conditions at the ice base. Due to the kilometre-thick ice cover, direct measurements in the bedrock are very difficult, and even precise information about the thermal regime of the ice base is limited to a few sites where deep ice cores have been drilled. Instead, several approaches exist to infer the GHF distribution under the ice sheet indirectly. Pollack *et al.*<sup>1</sup> provided a compilation of GHF measurements and derived a spherical-harmonic representation of the global GHF distribution to degree and order 12. Shapiro and Ritzwoller<sup>2</sup> used a global seismic model of the crust and the upper mantle to extrapolate these data under the ice sheets of Antarctica and Greenland. Fox Maule *et al.*<sup>3</sup> derived the GHF distribution for Greenland by combining magnetic measurements from satellites and a crustal magnetic field model. This distribution was later updated by Purucker<sup>4</sup>. More recently, Rezvanbehbahani *et al.*<sup>5</sup> combined geologic, tectonic and GHF data, and trained a machine learning algorithm on these data to provide a GHF distribution for Greenland.

These models differ greatly in the predicted distribution of the GHF. Rogozhina *et al.*<sup>6</sup> demonstrated that applying either of the distributions by Pollack *et al.*<sup>1</sup>, Shapiro and Ritzwoller<sup>2</sup> or Fox Maule *et al.*<sup>3</sup> for simulations of the Greenland ice sheet with the SICOPOLIS model (SIMulation CODE for POLYthermal Ice Sheets; [www.sicopolis.net](http://www.sicopolis.net)) does not reproduce the observed basal temperatures at the deep ice core locations. Therefore, there is an evident need for improvement.

Here, we present an update of the approach pursued by Greve<sup>7</sup> and Greve and Herzfeld<sup>8</sup>. The underlying idea is first to scale the spherical-harmonic representation by Pollack *et al.*<sup>1</sup> for Greenland, and then to modify the GHF values at the deep ice core locations such that a paleoclimatic simulation of the Greenland ice sheet with SICOPOLIS produces an optimum agreement between simulated and observed basal temperatures. A suitable interpolation algorithm combines the background representation of the GHF with the point data at the ice core sites. Compared to the two previous versions, we conduct an improved paleoclimatic simulation with 5 km horizontal resolution, add the NEEM ice core to the previously used cores (GRIP, Dye 3, Camp Century, NGRIP) and include GHF measurements from three bedrock boreholes.

## 2. Location

Our study area is the entire land area of Greenland, encompassing the ice sheet and ice-free land, and the surrounding oceans. Details on the domain, map projection and spatial resolution will be given below (Sects. 3, 4, Fig. 3).

## 3. Methods

### 3.1. Paleoclimatic simulation with SICOPOLIS

We use the dynamic/thermodynamic ice sheet model SICOPOLIS to conduct a paleoclimatic simulation of the Greenland ice sheet over the last glacial/interglacial cycle. The set-up is similar to the spin-up simulation described by Rückamp *et al.*<sup>9</sup> Viscous ice flow is described by the regularized Glen flow law given by Greve and Blatter<sup>10</sup>. The temperature-dependent rate factor for cold ice is by Cuffey and Paterson<sup>11</sup>, Sect. 3.4.6 and the water-content-dependent rate factor for temperate ice is by Lliboutry and Duval<sup>12</sup>. Basal sliding under grounded ice is described by a Weertman-type sliding law with sub-melt sliding in the form of Greve and Herzfeld<sup>8</sup> (with the reduced sliding parameter by Rückamp *et al.*<sup>9</sup>). Ice thermodynamics is modelled by the one-layer melting-CTS enthalpy scheme<sup>13</sup>. The main physical parameters are listed in Table 1.

The model domain for the Greenland ice sheet covers the entire area of Greenland and the surrounding oceans. We use the EPSG:3413 grid, based on a polar stereographic projection with the WGS 84 reference ellipsoid, standard parallel 70°N and central meridian 45°W. The stereographic plane is spanned by the Cartesian coordinates  $x$  and  $y$ , and the coordinate  $z$  points upward. The bed topography is BedMachine v3 (Ref.14). Glacial isostatic adjustment (GIA) is modelled by the local-lithosphere–relaxing-asthenosphere (LLRA) approach with a time lag  $\tau_{\text{iso}} = 3000$  a (Ref.15).

The stereographic plane is discretized by a regular grid with 5 or 10 km resolution. In the vertical, we use terrain-following coordinates (sigma transformation) with 81 layers in the ice domain and 41 layers in the thermal lithosphere layer below.

For the present-day mean annual and July mean surface temperature, we employ the parameterizations by Fausto *et al.*<sup>16</sup> These parameterizations express the temperature distributions as linear functions of surface elevation, latitude and longitude. However, the parameterizations are valid for 1996–2006, whereas our reference year (time  $t = 0$ ) is 1990. In order to correct for this difference, we apply an offset of  $-1^\circ\text{C}$  to both parameterizations. This value was estimated based on the data shown by Kobashi *et al.*<sup>17</sup>, Fig. 1 therein.

The main, time-dependent driver for the paleoclimatic simulation is the surface temperature anomaly  $\Delta T(t)$ , assumed to be spatially uniform over the Greenland ice sheet. It is based on the  $\delta^{18}\text{O}$  record from the NGRIP ice core<sup>18</sup> on the GICC05modelext time scale<sup>19</sup>, converted to temperature with the  $\Delta T/\delta^{18}\text{O}$  transfer factor of  $2.4^\circ\text{C} \text{‰}^{-1}$  by Nielsen *et al.*<sup>20</sup> (based on Huybrechts<sup>21</sup>). Warming during the Eemian is capped at

$\Delta T = +4.5^\circ\text{C}$  (otherwise, the Eemian Greenland ice sheet becomes unrealistically small). The record is extended into the penultimate glacial by assuming  $\Delta T = -20^\circ\text{C}$  at 140 ka b2k and a linear increase since then. For the most recent 4 ka, the surface temperature anomaly derived for the GISP2 site by Kobashi *et al.*<sup>17</sup> is used instead of the NGRIP record. The resulting temperature anomaly is shown in Fig. 1. In addition, we prescribe the sea level history, which is derived from the SPECMAP marine  $\delta^{18}\text{O}$  record<sup>22</sup>.

For the present-day precipitation, we use monthly means for the period 1958–2001, created with the regional energy and moisture balance model REMBO<sup>23</sup>. The horizontal resolution of the original data is 100 km. For any other time  $t$ , we assume a 7.3% change of the precipitation rate for every  $1^\circ\text{C}$  of surface temperature ( $\Delta T$ ) change<sup>21</sup>. Conversion from precipitation to snowfall rate (solid precipitation) is done on a monthly-mean basis using the empirical fifth-order polynomial function by Bales *et al.*<sup>24</sup> As in the study by Greve and Herzfeld<sup>8</sup>, surface melting is parameterized by Reeh's<sup>25</sup> positive degree day (PDD) method, supplemented by the semi-analytical solution for the PDD integral by Calov and Greve<sup>26</sup>. The PDD factors are  $\beta_{\text{ice}} = 8 \text{ mm w.eq. d}^{-1} \text{ }^\circ\text{C}^{-1}$  for ice melt and  $\beta_{\text{snow}} = 3 \text{ mm w.eq. d}^{-1} \text{ }^\circ\text{C}^{-1}$  for snow melt<sup>27</sup>. Furthermore, the standard deviation of short-term, statistical air temperature fluctuations is  $\sigma = 5^\circ\text{C}$ , and the saturation factor for the formation of superimposed ice is chosen as  $P_{\text{max}} = 0.6$  (Ref.25). In order to account for sub-grid-scale ice discharge into the ocean, we apply the discharge parameterization by Calov *et al.*<sup>28</sup>, Eq. (3) therein with the discharge parameter  $c = 370 \text{ m}^3 \text{ s}^{-1}$  for 5 km resolution and  $1270 \text{ m}^3 \text{ s}^{-1}$  for 10 km resolution.

We start the paleoclimatic simulation at  $t = -134 \text{ ka}$ , where  $\Delta T = -11.13^\circ\text{C}$ , which is close to the mean anomaly  $\overline{\Delta T}$  over the whole period (Fig. 1). In detail, the simulation consists of the following sequence of four runs:

- (1)  $t = -134 \dots -9 \text{ ka}$ , starting from the observed present-day topography, horizontal resolution 10 km, free evolution of the ice thickness, basal sliding ramped up during the first 5 ka.
- (2)  $t = 0 \dots 100 \text{ a}$ , starting from the observed present-day topography, horizontal resolution 5 km, no basal sliding, isothermal at  $-10^\circ\text{C}$ , ice extent constrained to present-day extent (purpose: to produce a slightly smoothed present-day topography of the Greenland ice sheet that serves as a target for the nudging technique of run (3)).
- (3)  $t = -9 \dots 0 \text{ ka}$ , horizontal resolution 5 km, reads the resolution-doubled output of run (1) for  $t = -9 \text{ ka}$  as initial condition, ice thickness continuously nudged towards the output of run (2) (slightly smoothed present-day topography) with a relaxation time of 100 a. This nudging is equivalent to applying a surface mass balance (SMB) correction<sup>29;30;31</sup>, which is diagnosed by the model.
- (4)  $t = -1 \dots 0 \text{ ka}$ , horizontal resolution 5 km, reads the output of run (3) for  $t = -1 \text{ ka}$ , free evolution of the ice thickness. The diagnosed SMB correction of run (3) for  $t = 0$  is employed as a temporally constant, prescribed correction.

The dynamic ( $\Delta t$ ) and thermodynamic ( $\Delta t_{\text{temp}}$ ) time steps are  $\Delta t = \Delta t_{\text{temp}} = 1 \text{ a}$  for the 10-km run (1) and  $\Delta t = \Delta t_{\text{temp}} = 0.5 \text{ a}$  for the 5-km runs (2)–(4).

### 3.2. Construction of the GHF map

The GHF constitutes the thermodynamic boundary condition at the bottom of the model domain. In order to account for the thermal inertia of the lithosphere, it is applied 2 km below the ice base<sup>32</sup>.

The method to construct the GHF map follows Greve<sup>7</sup> closely. We start with the spherical-harmonic representation to degree and order 12 of the global heat flux by Pollack *et al.*<sup>1</sup>, evaluated for our spatial domain around Greenland. The resulting distribution shows a general increase from west to east, but the

overall values are too high<sup>33</sup>. Therefore, in the first step, the distribution is scaled by a constant factor such that the mean heat flux for Greenland's land area (ice sheet and ice-free land) is reduced from  $\sim 78 \text{ mW m}^{-2}$  to  $60 \text{ mW m}^{-2}$ . This is equivalent to the scaling applied by Greve and Herzfeld<sup>8</sup>.

In the second step, the GHF map is modified as follows. For the  $N_m (= 1824)$  on the 5-km EPSG:3413 grid margin points of the numerical domain, designated by  $(x_n, y_n)$ ,  $n = 1 \dots N_m$ , the geothermal heat fluxes  $q_{\text{geo},n}$  of the above procedure are kept. For the  $N_c = 5$  ice-core locations  $(x_n, y_n)$ ,  $n = N_m + 1 \dots N_m + N_c$  (GRIP, Dye 3, Camp Century, NGRIP, NEEM), the geothermal heat fluxes  $q_{\text{geo},n}$  are chosen such that the simulated basal temperatures match the observed ones (see below). For the  $N_b = 3$  bedrock-borehole measurements at locations  $(x_n, y_n)$ ,  $n = N_m + N_c + 1 \dots N_m + N_c + N_b$  (SASS1, SASS2, GAP), the geothermal heat fluxes are prescribed as measured (Table 2). With these  $N = N_m + N_c + N_b$  reference points, the new GHF distribution  $q_{\text{geo}}(x, y)$  is computed by the weighted interpolation

$$q_{\text{geo}}(x, y) = \frac{\sum_{n=1}^N w_n(x, y) q_{\text{geo},n}}{\sum_{n=1}^N w_n(x, y)}. \quad (1)$$

The weighting factors  $w_n$  are taken as the squares of the inverse distances from the arbitrary position  $(x, y)$  to the reference points  $(x_n, y_n)$ ,

$$w_n(x, y) = \begin{cases} \frac{1}{N_m} \times \frac{1}{(x - x_n)^2 + (y - y_n)^2}, & n \leq N_m \text{ (margin point)}, \\ \frac{1}{(N_c + N_b)} \times \frac{1}{(x - x_n)^2 + (y - y_n)^2}, & n > N_m \text{ (ice-core or bedrock-borehole point)}. \end{cases} \quad (2)$$

The additional factors  $1/N_m$  and  $1/(N_c + N_b)$ , respectively, have been introduced in order to provide a balance between the influence of the large number of margin points and the small number of ice-core and bedrock-borehole locations.

The GHF values at the five ice-core locations are unknown. First, we run the simulation sequence described in Sect. 3.1 with the GHF map by Greve and Herzfeld<sup>8</sup>. The five values are then iteratively adjusted, depending on the misfit between measured and modelled basal temperatures at the ice-core locations, and the simulation sequence is re-run with the updated GHF map. Only integer GHF values are tested, and we stop the iteration when the optimum agreement is reached. For NGRIP and NEEM, this procedure does not produce unique GHF values because these sites are both warm-based (basal temperature at the pressure melting point). For NGRIP, we keep the value  $135 \text{ mW m}^{-2}$  already determined by Greve<sup>7</sup> and Greve and Herzfeld<sup>8</sup>, which leads to a large basal melting rate, in line with the estimate by Dahl-Jensen *et al.*<sup>34</sup> For NEEM, we determine a GHF value just sufficient to raise the basal temperature to the pressure melting point. The resulting GHF values and basal temperatures are listed in Table 2. They will be discussed further below (Sect. 5).

#### 4. Data Records

We provide the GHF distribution for Greenland that results from the iterative procedure explained above (Sect. 3.2) as gridded NetCDF (Network Common Data Form; [www.unidata.ucar.edu/software/netcdf](http://www.unidata.ucar.edu/software/netcdf)) files

on two different grids:

- EPSG:3413 grid:  
polar stereographic projection, WGS84 ellipsoid, standard parallel 70°N, central meridian 45°W, projection  $x$  coordinate  $-720$  km ...  $+960$  km, projection  $y$  coordinate  $-3450$  km ...  $-570$  km (e.g., Morlighem *et al.*<sup>14</sup>);
- Bamber grid:  
polar stereographic projection, WGS84 ellipsoid, standard parallel 71°N, central meridian 39°W, projection  $x$  coordinate  $-800$  km ...  $+700$  km, projection  $y$  coordinate  $-3400$  km ...  $-600$  km (e.g., Bamber *et al.*<sup>35</sup>).

On each grid, we provide the data in the three different resolutions (grid spacings) of 5 km, 10 km and 20 km. The data set therefore consists of six NetCDF files named

$$\text{GHF\_Greenland\_Ver2.0\_Gridxxx\_yykm.nc,}$$

where  $xxx \in \{\text{EPSG3413, Bamber}\}$  and  $yy \in \{05, 10, 20\}$ .

In addition to the geothermal heat flux (variable ‘GHF’, 2D array), each file contains the  $x$  coordinate (variable ‘x’, vector), the  $y$  coordinate (variable ‘y’, vector), the geographical latitude (variable ‘lat’, 2D array) and the geographical longitude (variable ‘lon’, 2D array). The data set is hosted by the Arctic Data archive System (ADS) of the National Institute of Polar Research (NIPR) in Tokyo, Japan (see “Data Citation” below).

If the GHF data are required on different resolutions or an unstructured mesh, we recommend resampling the data by bilinear interpolation.

## 5. Technical Validation

The evolution of the ice volume and area for the 134 ka paleoclimatic simulation (Sect. 3.1) with the optimized GHF distribution (Sect. 3.2) is shown in Fig. 2. The results are very similar to those obtained by Rückamp *et al.*<sup>9</sup> During the Eemian, a pronounced minimum occurs with an ice volume  $\sim 2$  m SLE less than today’s. During most of the last (Weichselian) glacial period, the entire available land area is glaciated, and on average  $\sim 1$  m SLE more ice than today is stored in the ice sheet. After  $t = -9$  ka, both the volume and the area drop rapidly, which is due to the nudging towards the (slightly smoothed) present-day topography that starts at this time with run (3) (see Sect. 3.1). For the final time  $t = 0$  (corresponding to the year 1990), the simulation produces a Greenland ice sheet with a volume of  $V_{\text{sim}} = 3.007 \times 10^6 \text{ km}^3$  (7.44 m SLE) and an area of  $A_{\text{sim}} = 1.855 \times 10^6 \text{ km}^2$ . These numbers agree very well with their observed counterparts,  $V_{\text{obs}} = 2.96 \times 10^6 \text{ km}^3$  (7.36 m SLE)<sup>35</sup> and  $A_{\text{obs}} = 1.801 \times 10^6 \text{ km}^2$  (Ref.36). The good agreement is mainly a consequence of the applied SMB correction in run (4) of the simulation sequence, and it is an essential prerequisite for adequately representing the dynamic and thermodynamic state of the present-day ice sheet.

Figure 3 shows the GHF distribution on the EPSG:3413 grid for the 5 km resolution. The underlying global representation by Pollack *et al.*<sup>1</sup> leads to, by trend, increasing GHF values from west to east. However, for the actual ice sheet, this trend is strongly superposed by the structure that results from the ice-core and bedrock-borehole data. GHF values are generally low in South Greenland and the north-western sector around and downstream of Camp Century. By contrast, the area around NGRIP and towards the north-east features elevated GHF values. These are likely related to Greenland’s passage over the Icelandic mantle plume tens of millions of years ago<sup>37</sup>. The area encompasses the entire North-East Greenland Ice Stream

(NEGIS), for which Fahnestock *et al.*<sup>38</sup> inferred locally very high basal melt rates (and thus GHF values) by analysing the internal layering detected by radar measurements. The general structure of the GHF distribution is quite similar to that inferred by Rezvanbehbahani *et al.*<sup>5</sup>, but differs greatly from the earlier reconstructions by Shapiro and Ritzwoller<sup>2</sup>, Fox Maule *et al.*<sup>3</sup> and Purucker<sup>4</sup>.

Due to the scarcity of the supporting points (five ice cores, three bedrock boreholes), the GHF distribution is strongly affected by their location. This is particularly pronounced for NGRIP, which is in the centre of a distinctive regional GHF maximum, whereas GRIP, Dye 3, Camp Century and GAP are in the centres of regional GHF minima. It is extremely unlikely that the real GHF distribution has its regional extrema exactly at these sites. Therefore, the strong imprint of the supporting points on the obtained GHF distribution is an artefact of the interpolation procedure that puts large weights on the GHF values at these sites (Eq. (2)). In general, we expect the real GHF distribution to feature more structure than the one shown in Fig. 3.

The basal temperatures that result from the paleoclimatic simulation are shown in Table 2. Comparing them (column  $T_b^{\text{sim}05}$ ) to their observed counterparts (column  $T_b^{\text{obs}}$ ) reveals that the iterative optimization produces a very good agreement, the residual mismatches being in the range of  $\sim 0.2^\circ\text{C}$ . Figure 4 displays the simulated distribution of the basal temperature for the entire area of Greenland. The large GHF values around NGRIP and in the entire northeastern sector of Greenland lead to widespread temperate conditions at the ice base. Temperate conditions also prevail in a large drainage system in central West Greenland, bounded approximately by Jakobshavn Ice Stream in the south and Rink Glacier in the north. In central East Greenland, cold conditions dominate the interior ice sheet, while temperate conditions occur directly under the fast-flowing ice streams and outlet glaciers (Kangerdlugssuaq Glacier etc.). The generally low GHF values in South Greenland entail a cold-based interior ice sheet with temperatures of  $-10^\circ\text{C}$  and less, whereas a discontinuous ring of temperate-based ice is found near the ice margin that, again, coincides with areas of fast ice flow.

We test the influence of horizontal resolution on the results by re-running steps (2) to (4) of the paleoclimatic simulation with 10 km instead of 5 km resolution, using the GHF distribution that results from the optimization done with the 5 km simulations. The obtained basal temperatures are also shown in Table 2 (column  $T_b^{\text{sim}10}$ ). Evidently, the influence of the resolution on the agreement is negligible. In other words, the optimized GHF distribution is the same (within integer accuracy for the five ice-core sites) for the two different resolutions.

## 6. Usage Notes

The GHF data product presented here has already been used in the study by Rückamp *et al.*<sup>9</sup> These authors conducted a paleoclimatic simulation with the SICOPOLIS model similar to the one described here (Sect. 3.1). Then, they used the result as an initial condition for comparative future-climate simulations with the two models SICOPOLIS and ISSM. They employed two different future-climate scenarios based on RCP2.6 projections from climate models, which are approximately in line with the limit of global warming negotiated for the Paris Agreement. The focus of their study was not so much on the actual results, but rather on the similarities and differences produced by the two models.

## 7. Competing Interests

The author declares no competing interests.

## 8. Figures

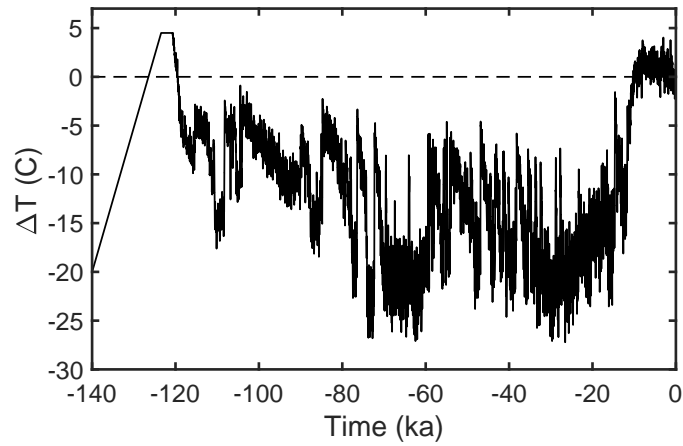


Figure 1: Surface temperature anomaly  $\Delta T(t)$  that results from the combination of the NGRIP record and that by Kobashi *et al.*<sup>17</sup> See main text for details (Sect. 3.1).

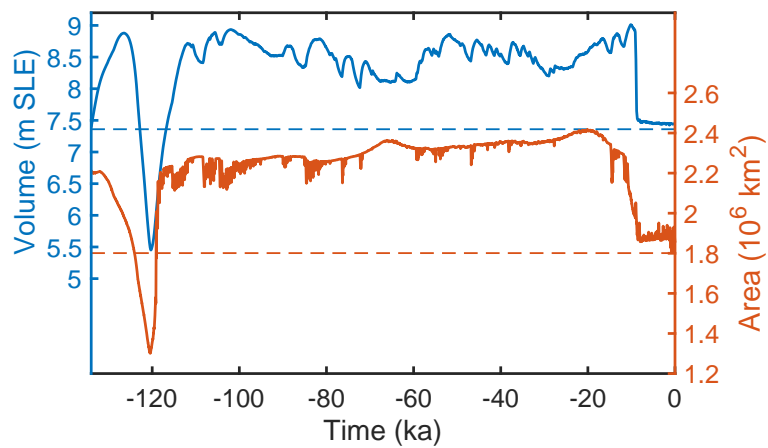


Figure 2: Ice volume (in m SLE = metres of sea-level equivalent) and area for the paleoclimatic simulation with SICOPOLIS: Run (1) before  $t = -9$  ka, run (3) between  $t = -9$  and  $-1$  ka, run (4) after  $t = -1$  ka (Sect. 3.1). Dashed lines indicate present-day values.

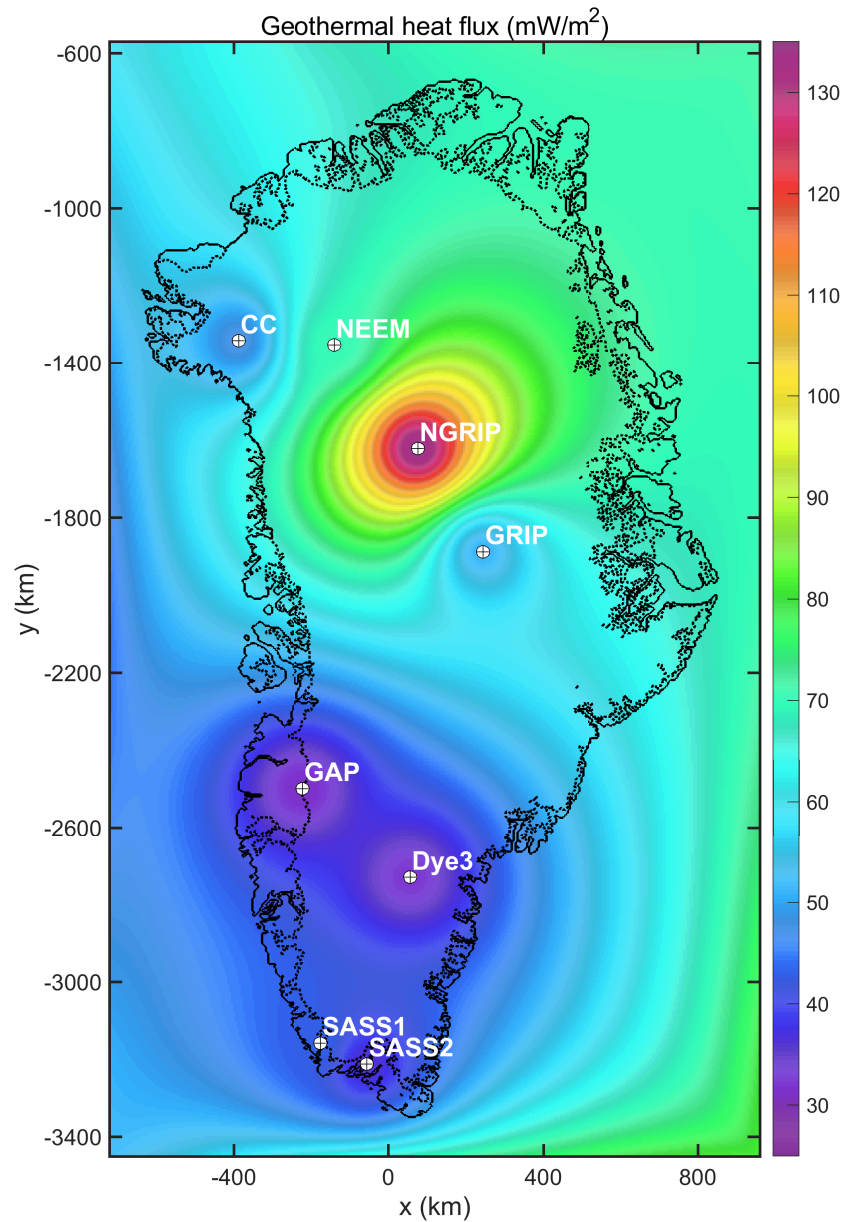


Figure 3: GHF map (in  $\text{mW m}^{-2}$ ) on the 5-km EPSG:3413 grid constructed by iteratively matching observed and simulated basal temperatures at the five ice core locations GRIP, Dye 3, Camp Century, NGRIP and NEEM. The bedrock-borehole sites SASS1, SASS2 and GAP are also shown. See main text for details (Sect. 3.2). Solid black line: land margin; dotted black line: ice margin.

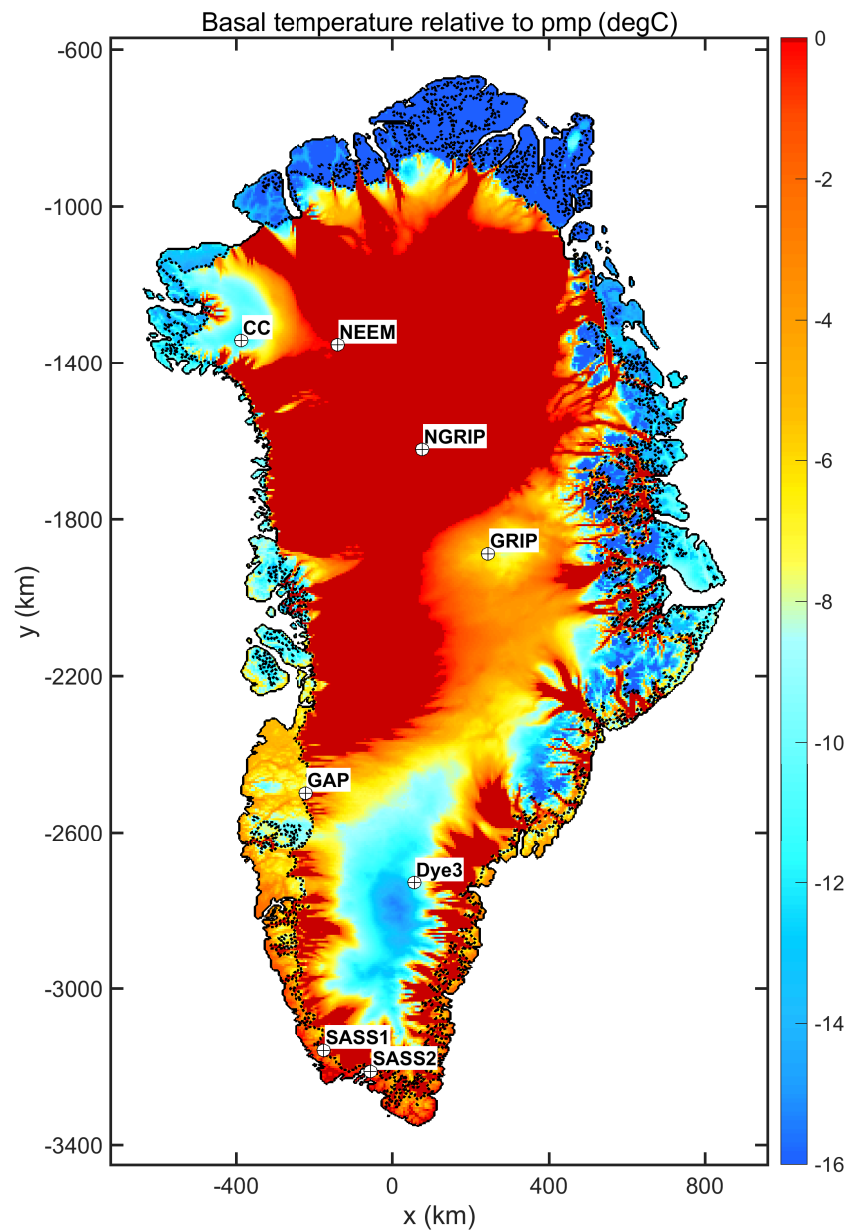


Figure 4: Basal temperature (relative to the pressure melting point, in °C) computed by the paleoclimatic simulation (Sect. 3.1) with the optimized GHF distribution (Fig. 3) on the 5-km EPSG:3413 grid. Solid black line: land margin; dotted black line: ice margin.

## 9. Tables

Quantity	Value
Density of ice, $\rho$	910 kg m <sup>-3</sup>
Gravitational acceleration, $g$	9.81 m s <sup>-2</sup>
Length of year, 1 a	31 556 926 s
Power law exponent, $n$	3
Residual stress, $\sigma_0$	10 kPa
Flow enhancement factor, $E$	1 / 3*
Melting temperature at low pressure, $T_0$	273.16 K
Clausius-Clapeyron gradient, $\beta$	$8.7 \times 10^{-4}$ K m <sup>-1</sup>
Universal gas constant, $R$	8.314 J mol <sup>-1</sup> K <sup>-1</sup>
Heat conductivity of ice, $\kappa$	$9.828 e^{-0.0057 T[\text{K}]} \text{ W m}^{-1} \text{ K}^{-1}$
Specific heat of ice, $c$	$(146.3 + 7.253 T[\text{K}]) \text{ J kg}^{-1} \text{ K}^{-1}$
Latent heat of ice, $L$	$3.35 \times 10^5 \text{ J kg}^{-1}$
Sliding coefficient, $C_b$	$6.72 \text{ m a}^{-1} \text{ Pa}^{-1}$
Sliding exponents, $(p, q)$	(3, 2)
Sub-melt-sliding parameter, $\gamma$	1°C
Asthenosphere density, $\rho_a$	3300 kg m <sup>-3</sup>
Density $\times$ specific heat of the lithosphere, $\rho_r c_r$	$2000 \text{ kJ m}^{-3} \text{ K}^{-1}$
Heat conductivity of the lithosphere, $\kappa_r$	$3 \text{ W m}^{-1} \text{ K}^{-1}$

Table 1: Physical parameters used for the simulations with SICOPOLIS (largely following ISMIP6 InitMIP-Greenland; Goelzer *et al.*<sup>39</sup>).

\*:  $E = 1$  for Holocene or Eemian ice (deposited between 11 ka BP and the present, or between 132 and 114 ka BP),  $E = 3$  for Weichselian or pre-Eemian ice (deposited during other times).

Site	Position (°N, °W)	$T_b^{\text{obs}}$ (°C)	$T_b^{\text{sim05}}$ (°C)	$T_b^{\text{sim10}}$ (°C)	GHF (mW m <sup>-2</sup> )
GRIP	72.57, 37.63	-8.56	-8.71	-8.71	51
Dye 3	65.19, 43.83	-13.22	-13.04	-13.18	32
Camp Century	77.17, 61.13	-13.00	-13.10	-13.12	47
NGRIP	75.10, 42.32	-2.4*	-2.65*	-2.65*	135
NEEM	77.50, 50.90	- ? * <sup>a</sup>	-2.18*	-2.18*	70
SASS1	61.40, 48.17	—	—	—	43
SASS2	60.97, 45.99	—	—	—	36
GAP	67.15, 50.07	—	—	—	31 <sup>b</sup>

Table 2: Observed and simulated (for 5 and 10 km resolution, respectively) basal temperatures,  $T_b$ , and inferred GHF at the five ice-core locations; measured GHF at the three bedrock-borehole locations.

References: GRIP: Dahl-Jensen *et al.*<sup>40</sup>; Dansgaard *et al.*<sup>41</sup>; NGRIP: North Greenland Ice Core Project members<sup>18</sup>; Dahl-Jensen *et al.*<sup>34</sup>; Camp Century: Dansgaard *et al.*<sup>42</sup>; Gundestrup *et al.*<sup>43;44</sup>; Dye 3: Gundestrup and Hansen<sup>45</sup>; NEEM: NEEM community members<sup>46</sup>; Goossens *et al.*<sup>47</sup>; SASS1, SASS2: Sass *et al.*<sup>48</sup>; GAP: Claesson Liljedahl *et al.*<sup>49</sup>

\*: Pressure melting point.

<sup>a</sup>: Precise value not yet published.

<sup>b</sup>: Mean of the values from two boreholes.

### Acknowledgements

The author thanks Dorthe Dahl-Jensen and Christine Schøtt Hvidberg (Univ. Copenhagen) for providing information about the NEEM ice core, Soroush Rezvanbehbahani (Univ. Kansas) for general discussions about the GHF of Greenland, and the two anonymous reviewers for useful comments on the manuscript.

This study was supported by Japan Society for the Promotion of Science (JSPS) KAKENHI grant numbers JP16H02224 and JP17H06104, and by the Arctic Challenge for Sustainability (ArCS) project of the Japanese Ministry of Education, Culture, Sports, Science and Technology (MEXT).

### References

1. Pollack, H. N., Hurter, S. J., Johnson, J. R. Heat-flow from the Earth's interior: Analysis of the global data set. *Rev. Geophys.* 1993, 31(3), p. 267–280.
2. Shapiro, N. M., Ritzwoller, M. H. Inferring surface heat flux distributions guided by a global seismic model: particular application to Antarctica. *Earth Planet. Sci. Lett.* 2004, 223(1-2), p. 213–224.
3. Fox Maule, C., Purucker, M. E., Olsen, N. Inferring magnetic crustal thickness and geothermal heat flux from crustal magnetic field models. Copenhagen, Denmark, Danish Meteorological Institute, 2009, Danish Climate Centre Report 08-01.
4. Purucker, M. E. Geothermal heat flux data set based on low resolution observations collected by the CHAMP satellite between 2000 and 2010, and produced from the MF-6 model following the technique described in Fox Maule *et al.* (2005). 2012. [http://websrv.cs.umt.edu/isis/index.php/Greenland\\_Basal\\_Heat\\_Flux](http://websrv.cs.umt.edu/isis/index.php/Greenland_Basal_Heat_Flux).
5. Rezvanbehbahani, S., Stearns, L. A., Kadivar, A., Walker, J. D., van der Veen, C. J. Predicting the geothermal heat flux in Greenland: A machine learning approach. *Geophys. Res. Lett.* 2017, 44(24), p. 12271–12279. <https://doi.org/10.1002/2017GL075661>.
6. Rogozhina, I., Hagedoorn, J. M., Martinec, Z., Fleming, K., Soucek, O., Greve, R., Thomas, M. Effects of uncertainties in the geothermal heat flux distribution on the Greenland Ice Sheet: An assessment of existing heat flow models. *J. Geophys. Res. Earth Surf.* 2012, 117(F2), F02025. <https://doi.org/10.1029/2011JF002098>.
7. Greve, R. Relation of measured basal temperatures and the spatial distribution of the geothermal heat flux for the Greenland ice sheet. *Ann. Glaciol.* 2005, 42, p. 424–432. <https://doi.org/10.3189/172756405781812510>.
8. Greve, R., Herzfeld, U. C. Resolution of ice streams and outlet glaciers in large-scale simulations of the Greenland ice sheet. *Ann. Glaciol.* 2013, 54(63), p. 209–220. <https://doi.org/10.3189/2013AoG63A085>.
9. Rückamp, M., Greve, R., Humbert, A. Comparative simulations of the evolution of the Greenland ice sheet under simplified Paris Agreement scenarios with the models SICOPOLIS and ISSM. *Polar Sci.* 2019. <https://doi.org/10.1016/j.polar.2018.12.003>. In press.
10. Greve, R., Blatter, H. *Dynamics of Ice Sheets and Glaciers*. Dordrecht, Springer, 2009, 287p., ISBN 978-3-642-03414-5. <https://doi.org/10.1007/978-3-642-03415-2>.
11. Cuffey, K. M., Paterson, W. S. B. *The Physics of Glaciers*. 4th edition, Amsterdam, Elsevier, 2010, 693p., ISBN 978-0-12-369461-4.
12. Lliboutry, L., Duval, P. Various isotropic and anisotropic ices found in glaciers and polar ice caps and their corresponding rheologies. *Ann. Geophys.* 1985, 3(2), p. 207–224.
13. Greve, R., Blatter, H. Comparison of thermodynamics solvers in the polythermal ice sheet model SICOPOLIS. *Polar Sci.* 2016, 10(1), p. 11–23. <https://doi.org/10.1016/j.polar.2015.12.004>.
14. Morlighem, M., Williams, C. N., Rignot, E., An, L., Arndt, J. E., Bamber, J. L., Catania, G., Chauché, N., Dowdeswell, J. A., Dorschel, B., Fenty, I., Hogan, K., Howat, I., Hubbard, A., Jakobsson, M., Jordan, T. M., Kjeldsen, K. K., Millan, R., Mayer, L., Mouginot, J., Noël, B. P. Y., O’Cofaigh, C., Palmer, S., Rysgaard, S., Seroussi, H., Siegert, M. J., Slabon, P., Straneo, F., van den Broeke, M. R., Weinrebe, W., Wood, M., Zinglensen, K. B. *BedMachine v3: Complete bed topogra-*

- phy and ocean bathymetry mapping of Greenland from multibeam echo sounding combined with mass conservation. *Geophys. Res. Lett.* 2017, 44(21), p. 11051–11061. <https://doi.org/10.1002/2017GL074954>.
15. Le Meur, E., Huybrechts, P. A comparison of different ways of dealing with isostasy: examples from modelling the Antarctic ice sheet during the last glacial cycle. *Ann. Glaciol.* 1996, 23, p. 309–317. <https://doi.org/10.3189/S0260305500013586>.
  16. Fausto, R. S., Ahlstrøm, A. P., Van As, D., Bøggild, C. E., Johnsen, S. J. A new present-day temperature parameterization for Greenland. *J. Glaciol.* 2009, 55(189), p. 95–105. <https://doi.org/10.3189/002214309788608985>.
  17. Kobashi, T., Kawamura, K., Severinghaus, J. P., Barnola, J.-M., Nakaegawa, T., Vinther, B. M., Johnsen, S. J., Box, J. E. High variability of Greenland surface temperature over the past 4000 years estimated from trapped air in an ice core. *Geophys. Res. Lett.* 2011, 38(21), L21501. <https://doi.org/10.1029/2011GL049444>.
  18. North Greenland Ice Core Project members. High-resolution record of Northern Hemisphere climate extending into the last interglacial period. *Nature.* 2004, 431(7005), p. 147–151. <https://doi.org/10.1038/nature02805>.
  19. Wolff, E. W., Chappellaz, J., Blunier, T., Rasmussen, S. O., Svensson, A. Millennial-scale variability during the last glacial: The ice core record. *Quaternary Sci. Rev.* 2010, 29(21–22), p. 2828–2838. <https://doi.org/10.1016/j.quascirev.2009.10.013>.
  20. Nielsen, L. T., Aðalgeirsdóttir, G., Gkinis, V., Nuterman, R., Hvidberg, C. S. The effect of a Holocene climatic optimum on the evolution of the Greenland ice sheet during the last 10 kyr. *J. Glaciol.* 2018, 64(245), p. 477–488. <https://doi.org/10.1017/jog.2018.40>.
  21. Huybrechts, P. Sea-level changes at the LGM from ice-dynamic reconstructions of the Greenland and Antarctic ice sheets during the glacial cycles. *Quaternary Sci. Rev.* 2002, 21(1–3), p. 203–231. [https://doi.org/10.1016/S0277-3791\(01\)00082-8](https://doi.org/10.1016/S0277-3791(01)00082-8).
  22. Imbrie, J., Hays, J. D., Martinson, D. G., McIntyre, A., Mix, A. C., Morley, J. J., Pisias, N. G., Prell, W. L., Shackleton, N. J. “The orbital theory of Pleistocene climate: Support from a revised chronology of the marine  $\delta^{18}\text{O}$  record”. *Milankovitch and Climate, Part I.* Berger, A., Imbrie, J., Hays, J., Kukla, G., Saltzman, B., eds. Dordrecht, D. Reidel Pub. Co., 1984, p. 269–305. (NATO ASI Series C: Mathematical and Physical Sciences, 126).
  23. Robinson, A., Calov, R., Ganopolski, A. An efficient regional energy-moisture balance model for simulation of the Greenland Ice Sheet response to climate change. *Cryosphere.* 2010, 4(2), p. 129–144. <http://doi.org/10.5194/tc-4-129-2010>.
  24. Bales, R. C., Guo, Q., Shen, D., McConnell, J. R., Du, G., Burkhart, J. F., Spikes, V. B., Hanna, E., Cappelen, J. Annual accumulation for Greenland updated using ice core data developed during 2000–2006 and analysis of daily coastal meteorological data. *J. Geophys. Res. Atmos.* 2009, 114(D6), D06116. <https://doi.org/10.1029/2008JD011208>.
  25. Reeh, N. Parameterization of melt rate and surface temperature on the Greenland ice sheet. *Polarforsch.* 1991, 59(3), p. 113–128.
  26. Calov, R., Greve, R. A semi-analytical solution for the positive degree-day model with stochastic temperature variations. *J. Glaciol.* 2005, 51(172), p. 173–175. <https://doi.org/10.3189/172756505781829601>.
  27. Huybrechts, P., de Wolde, J. The dynamic response of the Greenland and Antarctic ice sheets to multiple-century climatic warming. *J. Climate.* 1999, 12(8), p. 2169–2188. [https://doi.org/10.1175/1520-0442\(1999\)012<2169:TDR0TG>2.0.CO;2](https://doi.org/10.1175/1520-0442(1999)012<2169:TDR0TG>2.0.CO;2).
  28. Calov, R., Robinson, A., Perrette, M., Ganopolski, A. Simulating the Greenland ice sheet under present-day and palaeo constraints including a new discharge parameterization. *Cryosphere.* 2015, 9(1), p. 179–196. <https://doi.org/10.5194/tc-9-179-2015>.
  29. Aschwanden, A., Aðalgeirsdóttir, G., Khroulev, C. Hindcasting to measure ice sheet model sensitivity to initial states. *Cryosphere.* 2013, 7(4), p. 1083–1093. <https://doi.org/10.5194/tc-7-1083-2013>.
  30. Aschwanden, A., Fahnestock, M. A., Truffer, M. Complex Greenland outlet glacier flow captured. *Nat. Commun.* 2016, 7, 10524. <https://doi.org/10.1038/ncomms10524>.
  31. Calov, R., Beyer, S., Greve, R., Beckmann, J., Willeit, M., Kleiner, T., Rückamp, M., Humbert, A., Ganopolski, A. Simulation of the future sea level contribution of Greenland with a new glacial system model. *Cryosphere.* 2018, 12(10), p. 3097–3121. <https://doi.org/10.5194/tc-12-3097-2018>.

32. Ritz, C. “Time dependent boundary conditions for calculation of temperature fields in ice sheets”. *The Physical Basis of Ice Sheet Modelling*. Waddington, E. D., Walder, J. S., eds. Wallingford, UK, IAHS Press, 1987, p. 207–216, (IAHS Publication, No. 170).
33. Tarasov, L., Peltier, W. R. Greenland glacial history, borehole constraints, and Eemian extent. *J. Geophys. Res. Solid Earth*. 2003, 108(B3), 2143. <https://doi.org/10.1029/2001JB001731>.
34. Dahl-Jensen, D., Gundestrup, N., Gogineni, S. P., Miller, H. Basal melt at NorthGRIP modeled from borehole, ice-core and radio-echo sounder observations. *Ann. Glaciol.* 2003, 37, p. 207–212. <https://doi.org/10.3189/172756403781815492>.
35. Bamber, J. L., Griggs, J. A., Hurkmans, R. T. W. L., Dowdeswell, J. A., Gogineni, S. P., Howat, I., Mouginot, J., Paden, J., Palmer, S., Rignot, E., Steinhage, D. A new bed elevation dataset for Greenland. *Cryosphere*. 2013, 7(2), p. 499–510, <https://doi.org/10.5194/tc-7-499-2013>.
36. Kargel, J. S., Ahlstrøm, A. P., Alley, R. B., Bamber, J. L., Benham, T. J., Box, J. E., Chen, C., Christoffersen, P., Citterio, M., Cogley, J. G., Jiskoot, H., Leonard, G. J., Morin, P., Scambos, T., Sheldon, T., Willis, I. Brief communication: Greenland’s shrinking ice cover: “fast times” but not that fast. *Cryosphere*. 2012, 6(3), p. 533–537. <https://doi.org/10.5194/tc-6-533-2012>.
37. Rogozhina, I., Petrunin, A. G., Vaughan, A. P. M., Steinberger, B., Johnson, J. V., Kaban, M. K., Calov, R., Rickers, F., Thomas, M., Koulakov, I. Melting at the base of the Greenland ice sheet explained by Iceland hotspot history. *Nat. Geosci.* 2016, 9(5), p. 366–369. <https://doi.org/10.1038/NNGEO2689>.
38. Fahnestock, M., Abdalati, W., Joughin, I., Brozena, J., Gogineni, P. High geothermal heat flow, basal melt, and the origin of rapid ice flow in central Greenland. *Science*. 2001, 294(5550), p. 2338–2342. <https://doi.org/10.1126/science.1065370>.
39. Goelzer, H., Nowicki, S., Edwards, T., Beckley, M., Abe-Ouchi, A., Aschwanden, A., Calov, R., Gagliardini, O., Gillet-Chaulet, F., Golledge, N. R., Gregory, J., Greve, R., Humbert, A., Huybrechts, P., Kennedy, J. H., Larour, E., Lipscomb, W. H., Le clec’h, S., Lee, V., Morlighem, M., Pattyn, F., Payne, A. J., Rodehacke, C., Rückamp, M., Saito, F., Schlegel, N., Seroussi, H., Shepherd, A., Sun, S., van de Wal, R., Ziemen, F. A. Design and results of the ice sheet model initialisation experiments initMIP-Greenland: an ISMIP6 intercomparison. *Cryosphere*. 2018, 12(4), p. 1433–1460. <https://doi.org/10.5194/tc-12-1433-2018>.
40. Dahl-Jensen, D., Mosegaard, K., Gundestrup, N., Clow, G. D., Johnsen, S. J., Hansen, A. W., Balling, N. Past temperatures directly from the Greenland ice sheet. *Science*. 1998, 282(5387), p. 268–271. <https://doi.org/10.1126/science.282.5387.268>.
41. Dansgaard, W., Johnsen, S. J., Clausen, H. B., Dahl-Jensen, D., Gundestrup, N. S., Hammer, C. U., Hvidberg, C. S., Steffensen, J. P., Sveinbjörnsdóttir, A. E., Jouzel, J., Bond, G. Evidence for general instability of past climate from a 250-kyr ice-core record. *Nature*. 1993, 364(6434), p. 218–220. <https://doi.org/10.1038/364218a0>.
42. Dansgaard, W., Johnsen, S. J., Møller, J., Langway, C. C. One thousand centuries of climatic record from Camp Century on the Greenland ice sheet. *Science*. 1969, 166(3903), p. 377–380. <https://doi.org/10.1126/science.166.3903.377>.
43. Gundestrup, N. S., Clausen, H. B., Hansen, B. L., Rand, J. Camp Century survey 1986. *Cold Reg. Sci. Technol.* 1987, 14(3), p. 281–288. [https://doi.org/10.1016/0165-232X\(87\)90020-6](https://doi.org/10.1016/0165-232X(87)90020-6).
44. Gundestrup, N. S., Dahl-Jensen, D., Hansen, B. L., Kelty, J. Bore-hole survey at Camp Century 1989. *Cold Reg. Sci. Technol.* 1993, 21(2), p. 187–193. [https://doi.org/10.1016/0165-232X\(93\)90006-T](https://doi.org/10.1016/0165-232X(93)90006-T).
45. Gundestrup, N. S., Hansen, B. L. Bore-hole survey at Dye 3, South Greenland. *J. Glaciol.* 1984, 30(106), p. 282–288. <https://doi.org/10.3189/S0022143000006109>.
46. NEEM community members. Eemian interglacial reconstructed from a Greenland folded ice core. *Nature*. 2013, 493(7433), p. 489–494. <https://doi.org/10.1038/nature11789>.
47. Goossens, T., Sapart, C. J., Dahl-Jensen, D., Popp, T., El Amri, S., Tison, J.-L. A comprehensive interpretation of the NEEM basal ice build-up using a multi-parametric approach. *Cryosphere*. 2016, 10(2), p. 553–567. <https://doi.org/10.5194/tc-10-553-2016>.
48. Sass, J. H., Nielsen, B. L., Wollenberg, H. A., Munroe, R. J. Heat flow and surface radioactivity at two sites in South Greenland. *J. Geophys. Res.* 1972, 77(32), p. 6435–6444. <https://doi.org/10.1029/JB077i032p06435>.

49. Claesson Liljedahl, L., Kontula, A., Harper, J., Näslund, J.-O., Selroos, J.-O., Pitkänen, P., Puigdomenech, I., Hobbs, M., Follin, S., Hirschorn, S., Jansson, P., Kennell, L., Marcos, N., Ruskeeniemi, T., Tullborg, E.-L., Vidstrand, P. The Greenland Analogue Project: Final report. Stockholm, Sweden, Swedish Nuclear Fuel and Waste Management Company, 2016, Technical Report TR-14-13, 142p.

#### **Data Citation**

Greve, R. Geothermal heat flux distribution for the Greenland ice sheet, derived by combining a global representation and information from deep ice cores. 2.00, Arctic Data archive System (ADS), Japan, 2018, <https://doi.org/10.17592/001.2018022701>.